Check for
updates

Steady-State Transitions in Ordered Porous Media

T. O. M. Forslund[1] · **I. A. S. Larsson[1]** · **J. G. I. Hellström[1]** · **T. S. Lundström[1]**

Abstract
Previously performed experiments on flow through an ordered porous media cell with tomographic particle image velocimetry reveal a complex three-dimensional steady-state flow pattern. This flow pattern emerge in the region where inertial structures have been previously reported for a wide range of packings. The onset of these steady-state inertial flow structures is here scrutinized for three different types of packing using a finite difference method. It is concluded that the onset of the flow structure coincides with a symmetry break in the flow field and discontinuities in the pressure drop, volume averaged body forces and heat transfer. A quantity for identifying the transition is proposed, namely the pressure integral across the solid surfaces. It is also shown that the transition can both increase and decrease the heat transfer dependent on the actual geometry of the porous medium.

List of Symbols

L	Unit dimension of length
M	Unit dimension of mass
T	Unit dimension of time
Θ	Unit dimension of temperature
Ω	Fluid domain (L^3)
$\partial\Omega$	Fluid solid boundary (L^2)
ν	Kinematic viscosity (L^2T^{-1})
μ	Dynamic viscosity ($ML^{-1}T^{-1}$)
α	Thermal diffusivity (L^2T^{-1})
ρ	Density (ML^{-3})
t	Time coordinate (T)
x_i	Position coordinate vector (L)
u_i	Velocity vector (LT^{-1})
u	X-direction velocity component (LT^{-1})
v	Y-direction velocity component (LT^{-1})
w	Z-direction velocity component (LT^{-1})

✉ T. O. M. Forslund
  Tobias.Forslund@ltu.se

[1] Fluid and Experimental Mechanics, Luleå University of Technology, Luleå, Sweden

T	Temperature (Θ)
p	Pressure ($ML^{-1}T^{-2}$)
β	Compressibility factor ($ML^{-1}T^{-2}$)
U_{int}	Average speed of fluid inside pores (LT^{-1})
U_{Darcy}	Average speed of fluid averaged over solid and liquid phase (LT^{-1})
D_p	Obstruction diameter (L)
D_p	Obstruction radius (L)
L	Cell side length (L)
F_i	Momentum volume source ($ML^{-2}T^{-2}$)
F_δ	Norm of force gradient (MT^{-2})
S	Temperature source (ΘT^{-1})
T_G	Temperature gradient (ΘL^{-1})
p_{solid}	Average pressure at $\partial\Omega$ ($ML^{-1}T^{-2}$)
ϕ	Porosity
N_t	Number of timesteps
N_n	Number of viscosity values in sweep
Re	Reynolds number
Re_{Darcy}	Darcy velocity based Reynolds number
p^*	Dimensionless pressure drop
Pr	Prandtl number
Nu	Nusselt number
Nu_{avg}	Average Nusselt number at $\partial\Omega$
$\bar{T}$	Time average of T
$< T >$	Spatial average of T
T'	Fluctuating value of T
$\lvert T\rvert$	Absolute value of T
$\lvert T_i\rvert$	Norm of vector T_i
$T_{,i}$	$\left(\dfrac{\partial T}{\partial x_i}\right)$
$\sigma(T)$	Spatial standard deviation of T

1 Introduction

Porous media flow takes place in many natural and industrial processes including flow through soils, aquifers, oil and gas reservoirs (Bear 1972), textiles (filters, for instance), biological tissues and plants. Other examples are flow through fuel cells (Farzaneh et al. 2021), cooling of batteries Moosavi et al. (2021), flow during composites manufacturing (Lu et al. 2017; Tan and Pillai 2012a, b, c),industrial wicks (Zarandi et al. 2022) flow during paper-making, drying of iron ore pellets (Burstrom et al. 2018), internal erosion in embankment dams (Frishfelds et al. 2011), heat exchangers (Odabaee and Hooman 2012) and in-tissue drug delivery. This long list of applications (although it is not by far complete) points out that it is of utmost importance to increase the understanding of different flow structures present in various kinds of porous media. Increased knowledge will enable an optimization of the properties of the porous media as well as the parameters governing the flow. As to Reynolds number the flow in porous media is usually subdivided into four regions, these are called the *Darcy region*, *laminar steady region*, *laminar unsteady region*

and *turbulent region*. The regions are defined by the following flow conditions being observed (Seguin et al. 1998a, b):

- Darcy - $p_{,i} \propto u_i$,
- Laminar steady - $\frac{\partial u_i}{\partial t} = 0$,
- Laminar unsteady - $\frac{\partial u_i}{\partial t} \neq 0$ without turbulent cascade,
- Turbulent - $\frac{\partial u_i}{\partial t} \neq 0$ with turbulent cascade.

Where $p_{,i}$ denotes $\frac{\partial p}{\partial x_i}$. In addition other categories for flow through porous media can be identified including Newtonian or Non-Newtonian behaviour, single and multi-phase flow, wicking and saturated flow and free or confined flow, e.g. (Xu and Pillai 2017; Larsson et al. 2018; Jouybari and Lundstrom 2021). In this study Newtonian, single-phase, incompressible, low Knudsen number, saturated confined flow is considered.

The different regions as to Reynolds number have been considered in a number of studies with focus on different types of porous media. To exemplify, for turbulent flow through ordered arrays the particle shape and the type of array are crucial for how important different turbulent quantities are (Yang et al. 2014) and the heat flux due to thermal dispersion and turbulence is small as compared to the convective contribution (Jouybari et al. 2020). Plots from the same study also show that the heat flux caused by turbulence is limited to single pores confirming that the size of turbulent structures in porous media is generally limited to the pore scale, leading to the pore-scale prevalence hypothesis (Jin et al. 2015; Uth et al. 2016). Only for a limited range of porosities $\phi > 0.93$ and Darcy numbers, the turbulence structures can extend to nearby pores (Rao and Jin 2022). Randomly packed beds of spheres is another type of porous medium that has been scrutinized. With focus on turbulence, results in (Patil and Liburdy 2013) show that the characteristics of the turbulence is nearly the same between pores. In (Nguyen et al. 2018) comparisons between velocities and the Reynolds stresses yield an increase in turbulent intensity and the mixing within the pores when the Reynolds number is increased. In (Khayamyan et al. 2017a, 2017b) also flow through randomly packed beds is studied but with focus on the laminar unsteady region. From Stereoscopic Particle Image Velocimetry it is, for instance, shown that the spatial variation in the time averaged absolute velocity increases with particle Reynolds number up to about 410 and then the variation decreases (Khayamyan et al. 2017). This is explained with a transition from the laminar unsteady to the turbulent region. A similar observation is reported in Johns et al. (2000) who analyzed inertial transitions in packed beds by using magnetic resonance imaging. The spatial variance of velocity decreases considerably at a local (pore) Reynolds number of about 30. The mechanisms is, however, likely to be different to that in Khayamyan et al. (2017) since the decrease with Reynolds number in Johns et al. (2000) takes place in the laminar steady regime. Scrutinizing the results in Khayamyan et al. (2017), in detail (Figures 9, 10), the spatial variation in velocity actually decreases when the Reynolds number increases between 20 and 40 (before the variation increases up to Reynolds number 410). This is in the laminar steady flow region for this geometry and therefore in-line with the results in Johns et al. (2000) indicating that the epsilon shaped effect is a generic feature.

In the above discussion, a few values of the Reynolds number are mentioned. It should however be stated that the transitional Reynolds numbers are crucially dependent on the geometry studied. This will also be the case for the onset of the flow structures examined in this study. For porous media flow, the different types of Reynolds numbers used in the literature can complicate comparisons to actual Reynolds numbers even more.

This study focuses on a type of inertial flow structure observed in the laminar steady flow region for saturated Newtonian single phase flow through structured porous media. The epsilon-shaped effect studied inhere, was first observed in a previous work by the authors of this article when studying the flow through a porous medium consisting of pillars placed between two parallel horizontal and two parallel vertical plates see Fig. 1 (Forslund et al. 2021). The effect is named the epsilon effect due to the epsilon-shaped inertial cores that are formed for this particular geometry. Based on data available it is concluded that the structure is caused by wall interactions and that it remains steady as long as the Reynolds number is kept constant. Numerical simulations later confirmed that a similar, albeit distinct, flow structure could arise independent of wall interactions. In this study, a finite difference method (FDM) solver is utilized and the onset of the effect is scrutinized to yield a greater insight into the underlying mechanisms. The results show that for high-tortuosity porous media, an inertial-viscous transition occurs that is characterized by a breakdown of the high pressure region on the impinging surfaces. The transition manifests as a symmetry break in the flow field with inertial cores that are directed around the obstructing geometry. It is also shown that the transition occurs in packings of spheres.

2 Theory

The full Navier–Stokes equations on tensor form reads

$$\rho\left(\frac{\partial u_i}{\partial t} + u_j u_{i,j}\right) = -p_{,i} + \rho \nu u_{i,jj} + F_i \tag{1}$$

where u_i is the velocity vector, ρ is the density, ν is the kinematic viscosity and F_i is some external body force term like gravity on volume density form. For steady-state flows the transient flow field variation is zero, i.e. $\frac{\partial u_i}{\partial t} = 0$. These two measures simplify Eq. (1) to

Fig. 1 The epsilon effect as observed experimentally by tomographic PIV measurements, the green planes indicates the position of the slices in the porous cell. Inlet is to the left and outlet to the right with the flow direction along the positive x-axis. The pillars seen are placed between two parallel horizontal and two parallel vertical walls. Further details are available in Forslund et al. (2021)
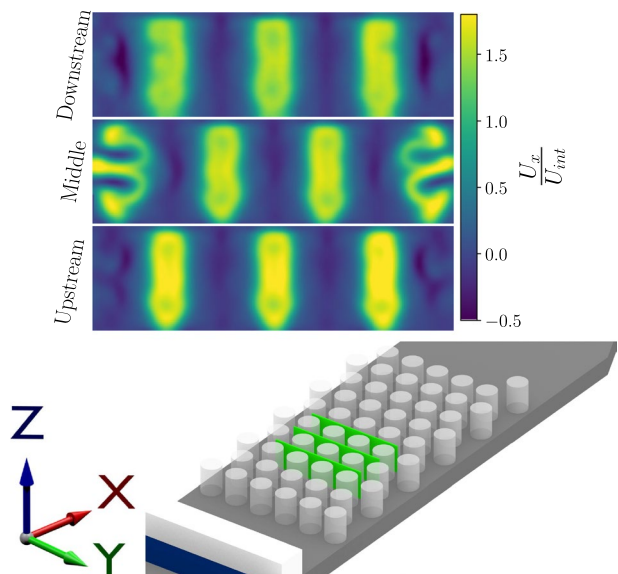
$$\rho u_j u_{i,j} + p_{,i} - \rho v u_{i,jj} = F_i.$$ (2)

From left to right the above terms are referred to as the *inertial term*, *static pressure term*, *viscous drag term* and the *source term*. Integrating this expression over the fluid domain Ω gives the average contribution of each term

$$
\begin{aligned}
\rho \left(\int_\Omega d\Omega \right)^{-1} &\left(\int_\Omega u_j u_{i,j} d\Omega + \int_\Omega \frac{1}{\rho} p_{,i} d\Omega - \int_\Omega v u_{i,jj} d\Omega \right) \\
&= \left(\int_\Omega d\Omega \right)^{-1} \left(\int_\Omega F_i d\Omega \right).
\end{aligned}
$$ (3)

These quantities are referred to as *spatially averaged* terms and is the average force balance in the fluid domain. In this study periodic boundary conditions are applied, this implies that the entire fluid domain consists of closed steady-state streamlines. Therefore the spatially averaged value of the convective term $\int_\Omega u_j u_{i,j}$ is zero, and Eq. (3) is reduced to

$$
\begin{aligned}
\rho \left(\int_\Omega d\Omega \right)^{-1} &\left(\int_\Omega \frac{1}{\rho} p_{,i} d\Omega - \int_\Omega v u_{i,jj} d\Omega \right) \\
&= \left(\int_\Omega d\Omega \right)^{-1} \left(\int_\Omega F_i d\Omega \right).
\end{aligned}
$$ (4)

If the pressure gradient term is significantly larger than the viscous term, the flow is said to be *inertially limited*. Another useful quantity is the volume averaged force magnitudes defined by

$$
\begin{aligned}
< |F_p| > &= \left(\int_\Omega d\Omega \right)^{-1} \left(\int_\Omega \sqrt{p_{,i} p_{,i}} d\Omega \right), \\
< |F_v| > &= \rho \left(\int_\Omega d\Omega \right)^{-1} \left(\int_\Omega v \sqrt{u_{i,jj} u_{i,kk}} d\Omega \right), \\
< |F_{\text{conv}}| > &= \rho \left(\int_\Omega d\Omega \right)^{-1} \left(\int_\Omega \sqrt{u_j u_{i,j} u_k u_{i,k}} d\Omega \right).
\end{aligned}
$$ (5)

These quantities give an idea of how much the average local force balance varies between the computational elements.

2.1 Dimensionless Numbers

2.1.1 Reynolds Number

The Reynolds number characterizes the flow-dynamics of the hydrodynamic phase, here defined as

$$\text{Re} = \frac{U_{\text{int}} D_p}{v}.$$ (6)

Where U_{int} is the *interstitial velocity* defined as the average streamwise velocity in the fluid, D_p is the obstruction diameter and v is the kinematic viscosity as introduced earlier. This

definition of the Reynolds number will be used in the analysis. For comparison to earlier works the Darcy-velocity-based Reynolds number is used, defined as

$$\mathrm{Re}_{\mathrm{Darcy}} = \frac{U_{\mathrm{Darcy}} D_p}{\nu}. \tag{7}$$

The value of U_{Darcy} is related to the interstitial velocity via $U_{\mathrm{int}} = U_{\mathrm{Darcy}}/\phi$, where ϕ is the porosity.

2.1.2 Prandtl Number

The Prandtl number is defined as the ratio of the viscous diffusion to the thermal diffusion

$$\mathrm{Pr} = \frac{\nu}{\alpha}. \tag{8}$$

2.1.3 Dimensionless Pressure Drop

The dimensionless pressure drop, p^*, can be interpreted as a dimensionless measure of the deviation from Darcy's law for non-Stokesian flow. If p^* is constant with respect to the Reynolds number then the pressure drop increases linearly with velocity. This expression can be written as Lundstrom et al. (2010)

$$p^* = \frac{|F_i| R^2}{\mu U_{\mathrm{int}}}. \tag{9}$$

Here R is a reference length scale, which in this work is set to the radius of the obstructions, $|F_i|$ is the norm of the force density, i.e. the body force acting on each unit volume, and μ is the dynamic viscosity.

2.1.4 Nusselt Number

The Nusselt number Nu is a dimensionless measure of the heat transfer between the solid phase and the fluid phase defined as Foudhil et al. (2012)

$$\mathrm{Nu} = \left(\frac{\partial T}{\partial n} \right)_{n=\partial \Omega} \frac{L}{T_{fm} - T_{fw}}. \tag{10}$$

In this expression T is the temperature, n is the normal pointing out from the wall at the fluid solid boundary $\partial \Omega$, L is some length scale, here set to the obstruction diameter $L = 2R$. T_{fw} is the wall temperature and T_{fm} is the bulk temperature defined by

$$T_{fm} = \frac{\int_\Omega T u_x \mathrm{d}\Omega}{\int_\Omega u_x \mathrm{d}\Omega}, \tag{11}$$

Where u_x is the streamwise velocity. For all cases discussed in this article $T_{fw} \equiv 0$ which simplifies the expression for the Nusselt number to

$$\mathrm{Nu} = \left(\frac{\partial T}{\partial n}\right)_{n=\partial\Omega} \frac{2R \int_\Omega u_x \mathrm{d}\Omega}{\int_\Omega Tu_x \mathrm{d}\Omega}. \tag{12}$$

The average Nusselt number taken across the entire boundary $\partial\Omega$ can then be written as

$$Nu_{\mathrm{avg}} = \frac{\int_{\partial\Omega} \left(\frac{\partial T}{\partial n}\right)_{n=\partial\Omega} \frac{2R \int_\Omega u_x \mathrm{d}\Omega}{\int_\Omega Tu_x \mathrm{d}\Omega} \mathrm{d}(\partial\Omega)}{\int_{\partial\Omega} \mathrm{d}(\partial\Omega)}. \tag{13}$$

3 Method

3.1 Numerical Method

An in-house finite difference, artificial compressibility solver with explicit time-stepping is utilized for the numerical analysis. The code is available under a free license at https://gitlab.com/c8383/gpu-fdm and further technical details regarding the implementation of the model is available in the repository. In addition to this, the discretization is described in detail in Appendix A. There are alternative models known to the authors such as LBM (Abbaszadeh et al. 2017; Forslund et al. 2021) and FVM methods (Lundstrom et al. 2010); the model in this work was chosen based on the simplicity of the discretization scheme which provides full insight into the flow field update procedure, which is essential to this study. Since the aim is to solve the equations for a fluid, Navier–Stokes equations are applied. The momentum balance hence becomes

$$\frac{\partial u_i}{\partial t} + u_j u_{i,j} = -\frac{1}{\rho} p_{,i} + \nu u_{i,jj} + \frac{1}{\rho} F_i. \tag{14}$$

The standard continuity condition ($u_{i,i} = 0$) is replaced by an artificial compressibility condition (Kwak and Kiris 2011)

$$\frac{\partial p}{\partial t} + \beta u_{i,i} = 0. \tag{15}$$

Where β is the compressibility factor. A known problem for collocated grids are checkerboarding (Ferziger et al. 2002), in this solver the checkerboarding is reduced by a pressure field smoothing operation which increases neighboring cell interactions, the expression for the smoothing operation is

$$\frac{\partial p}{\partial t} + S_p p_{,ii} = 0, \tag{16}$$

where S_p is some smoothing factor. The thermal distribution is governed by the convection-diffusion equation

$$\frac{\partial T}{\partial t} + u_j T_{,j} = \alpha T_{,jj} + S, \tag{17}$$

where T is the temperature, α is the thermal diffusivity, and S is a source term. The density is set to unit $\rho = 1\mathrm{ML}^{-3}$ for all calculations.

3.2 Temporal and Spatial Discretization

The spatial discretization is second-order accurate and utilizes central derivatives for all relevant quantities, i.e. if ϕ is some field variable then the second- and first-order derivatives are given by

$$\frac{\mathrm{d}\phi}{\mathrm{d}x_i} = \frac{(\phi_{i+1} - \phi_{i-1})}{2\Delta x_i} + O(\Delta x_i^2), \tag{18}$$

$$\frac{\mathrm{d}^2\phi}{\mathrm{d}x_i^2} = \frac{(\phi_{i+1} - 2\phi_i + \phi_{i-1})}{\Delta x_i^2} + O(\Delta x_i^2). \tag{19}$$

The computational kernel consists of seven neighboring interacting elements as visualized in Fig. 2. The temporal discretization is first-order accurate and utilizes a simple Euler-forward scheme, i.e. the value of the field variable ϕ at time $t + 1$ is only dependent on field variables at time t

$$\phi^{t+1} = \phi^t + \Delta t \mathbf{f} + O(\Delta t). \tag{20}$$

Here $\mathbf{f}$ is a general function which includes any field values at time t within the computational kernel. To ensure that the compressibility effects are minimal the Mach number, defined as cell velocity over sound velocity U/U_c, should be kept at a low value (Kwak and Kiris 2011).

3.3 Computational Grid

The nodes are spaced equidistantly in all directions ($\Delta x = \Delta y = \Delta z = 1$) across a lattice of size $n_x \times n_y \times n_z$. The nodes are then set as either wall elements or fluid elements, i.e. the geometry is approximated using the stepwise approximation as described in Ferziger et al. (2002).

Fig. 2 The computational kernel for the FDM solver, all field values ϕ are collocated. The colored spheres indicates the node centers in the different coordinate directions x (red), y (green) and blue (z)
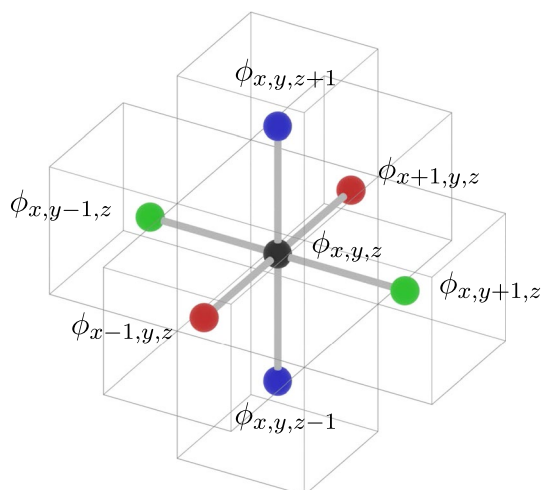
3.4 Verification of Numerical Method

To ensure that the FDM model is accurate it is verified against two cases. For the thermal part the model is compared against an analytical solution for a heated channel case derived by Rybiński and Mikielewicz (2014). For the porous media part the dimensionless drag is compared to the simulations of Koch and Ladd (1997).

3.4.1 Thermal Plane Channel Flow

The thermal channel verification case, see Fig. 3 for the geometry, consists of a plane channel of dimensions a, b with constant temperature walls (T_w), and a driving force (F_x). The temperature gradient in the streamwise direction is specified as some value $\frac{dT}{dx} = T_G$. For this case the following analytical solution for the velocity was derived by Rybiński and Mikielewicz (2014)

$$
u_x(z,y) = \frac{F_x}{\mu} \left[\frac{1}{2} \left(y^2 - \frac{b^2}{4} \right) + \ldots \right.
$$
$$
\left. - 4b^2 \sum_{n=1}^{\infty} \frac{(-1)^n}{C_n^3} \frac{\cosh\left(C_n K \frac{z}{a} \right)}{\cosh\left(C_n K \frac{1}{2} \right)} \cos\left(C_n \frac{y}{b} \right) \right].
$$
(21)

Where $C_n = (2n-1)\pi$ and $K = a/b$. The analytical expression for the temperature is given by

$$
T(x,y) = T_w + \frac{F_x T_G}{\alpha \mu} \left\{ \frac{1}{8} \left(\frac{y^4}{3} - \frac{b^2 y^2}{2} + \frac{5b^4}{48} \right) + \ldots \right.
$$
$$
+ 2b^4 \sum_{n=1}^{\infty} \frac{(-1)^n}{C_n^5} \left[2 + C_n K \frac{1}{2} \tanh\left(C_n K \frac{1}{2} \right) + \ldots \right.
$$
$$
\left. - C_n K \frac{z}{a} \tanh\left(C_n K \frac{z}{a} \right) \right] \times \frac{\cosh\left(C_n K \frac{z}{a} \right)}{\cosh\left(C_n K \frac{1}{2} \right)} \cos\left(C_n \frac{y}{b} \right) \right\}.
$$
(22)

The calculation input values are summarized in Table 1, N_t is the amount of time-steps before data is saved. The FDM model agrees perfectly with the analytical expression for the cases of velocity and temperature, see Fig. 4.

Fig. 3 Geometry of the plane channel used for thermal verification case
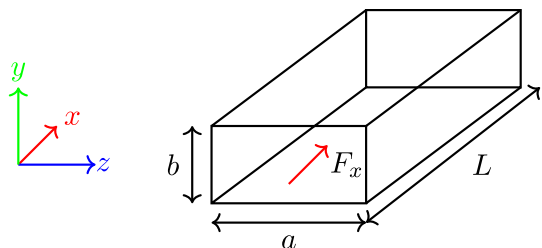
3.4.2 Porous Media Flow

The porous media verification case consists of an ordered cubic array of cylinders with the REV being a single quadratic elementary cell of side length L and cylinder diameter D_p, see Fig. 5. The flow is driven by a force gradient, F_δ, which results in an average stream-wise Darcy velocity, U_{Darcy}, that can be used to calculate the dimensionless drag, $\frac{F_\delta}{\mu U_{\text{Darcy}}}$, and the Reynolds number, $\text{Re}_{\text{Darcy}} = \frac{U_{\text{Darcy}} D_p}{\nu}$. The calculation input values are summarized in Table 2, N_t is the amount of time-steps before data is saved for each viscosity, N_n is the amount of viscosities, $\nu(n)$ is the viscosity for sweep number n starting from $n = 0$ and ending at $n = N_n - 1$. The FDM model agrees excellently with the computations carried out by Koch and Ladd (1997) throughout the inertial region and into the unsteady region ($\text{Re}_{\text{Darcy}} > 150$) as well, see Fig. 6.

4 Results

Three different types of porous media are investigated, see Fig. 7 for the geometries and the meshes. These are a staggered array of cylinders, in which the epsilon-shaped, inertial flow structure of interest here was first discovered, a staggered array of rods with a quadratic cross section, and a body-centered cubic (BCC) packing of spherical obstructions. The boundary conditions for the cells are periodic in all directions x, y and z where the wall elements are defined using a stepwise approximation, marked to the right in Fig. 7. The obstruction diameter D_p is the width of the obstruction and ϕ is the resulting porosity from the stepwise approximation. The flow is driven by a body force in the x-direction, F_x, and the viscosity is varied to investigate how the properties of the bed changes with Reynolds number. For all cases, the temperature of the wall elements is set to zero and a constant temperature source, S, is applied to all fluid elements. This method of obtaining the Nusselt number is described by Chu et al. (2019) who use a varying temperature source to enforce a constant heat flux, for a steady-state temperature field the source term S can be specified as a constant. An N_t amount of time steps are calculated for each viscosity to allow all flow field variables to reach a steady-state. See Table 3 for a summary of the simulation parameters for each case. A grid sensitivity analysis is presented in Appendix B. The variation of

Parameter	Value
$(n_x \times n_y \times n_z)$	$(128 \times 64 \times 64)$
ν	0.045
α	0.045
β	0.0125
F_x	3×10^{-5}
T_G	5×10^{-8}
T_w	0
Δt	1
N_t	100000

Table 1 Summary of the specified simulation parameters used for the thermal plane channel flow verification case

Fig. 4 Comparison between analytical (Rybiński and Mikielewicz 2014) and FDM solution for thermal channel flow
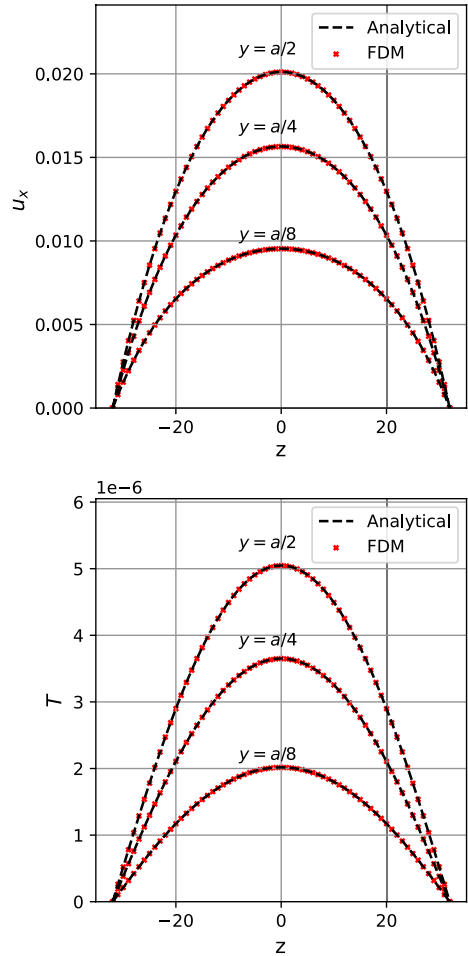
the dimensionless pressure drop p^* with Re is presented in Fig. 8, it can be seen how the value of p^* tends to a constant value for low Re Darcian flow.

4.1 Flow Field Changes

For all geometries investigated a discontinuity is observed in a multitude of variables at a Reynolds number specific to each packing type. This discontinuity is accompanied by a dramatic change in the flow field as exemplified with the velocity fields in Fig. 9. For the staggered cylinder and staggered rod cases the flow field exhibits a symmetry break with the emergence of complex 3D flow structures. The value of Re where the structure appears coincides with the value in the experimental work presented in Forslund et al. (2021), appearing at an Re of ≈ 80. For the BCC packing there are two separate transitions, one occurring at Re = 150 and a second one occurring at Re $\approx 230 - 250$. Since the transitions are triggered by an increase in Re it is assumed that they are caused by inertial forces starting to dominate over viscous forces.

Fig. 5 Porous media geometry for the verification. The parametrization (top) and mesh (bottom). Red and green boundaries are respectively connected by periodic boundary conditions
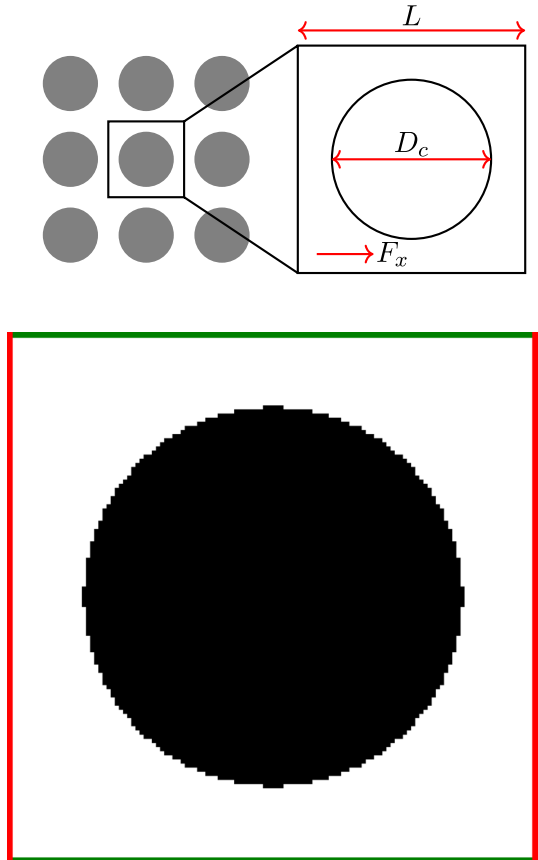

As mentioned in the introduction (Johns et al. 2000) analyzed inertial transitions in packed beds by using magnetic resonance imaging and found an inertial transition characterized by a decrease in the spatial standard deviation of velocity with Reynolds number. Indications of such a behaviour can also be seen in (Khayamyan et al. 2017). Hence, for comparison to these observations plots of the standard deviation of velocity taken over the fluid phase for the current geometries are presented in Fig. 10. For the staggered cylinder and staggered rod cases a clear reduction of the spatial variation of velocity can be seen at the transition as indicated by the vertical lines. For the BCC

Table 2 Summary of the specified simulation parameters for the porous media flow verification case

Parameter	Value
$(n_x \times n_y \times n_z)$	$(128 \times 128 \times 2)$
$v(n)$	$0.095/(3n + 1)$
β	0.0125
F_x	5.3×10^{-7}
Δt	1
N_t	100000
N_n	10

Fig. 6 Comparison between the computational results in Koch and Ladd (1997) and results from the FDM code for porous media flow (top). There is an excellent agreement. Visualization of flow regions (bottom), from left to right, Stokes region, inertial steady and inertial unsteady
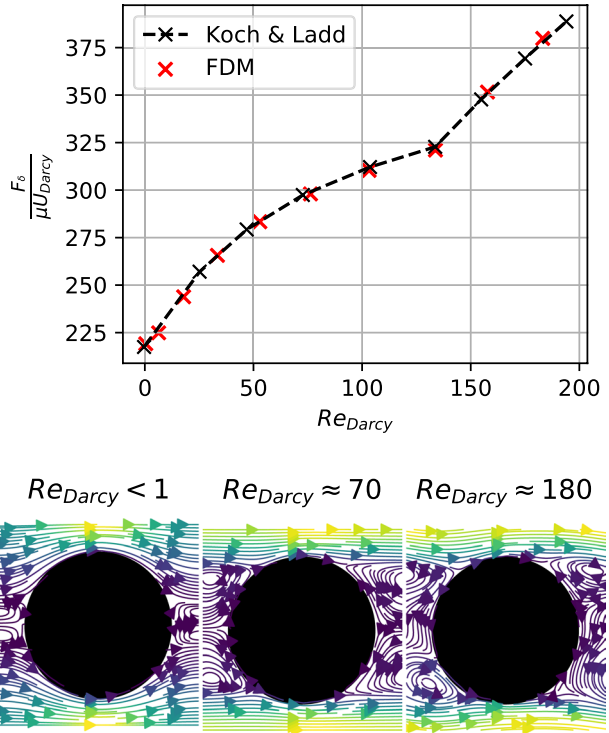
packing a clear and dramatic reduction is observed for the first transition (red line) and there is also a minor change in the shape of the curve at the second transition (blue line). This indicates that the inertial transition calculated for these geometries is of the same type that has been observed earlier, characterized by a decrease in the spatial standard deviation.

4.2 Pressure Drop and Force Balance

In Fig. 11 the dimensionless pressure drop, as defined by Eq. (9), is plotted against Re for the staggered cylinder, staggered quadratic rod and BCC cases. At $Re \approx 85, 65, 250$, respectively, the pressure drop variation exhibits a sharp but small discontinuity accompanied by the aforementioned changes in the flow field that can be seen in Fig. 9. The transitions correlate with changes in the signed volume averaged forces as can be seen in Fig. 12 for the staggered cubic rods and BCC cases. However, the near non-existent change for the staggered cylinder case indicates that the streamwise volume-averaged ratio of pressure gradient to viscous forces is not a good general indicator of transition. The transitions also correlate with a significant change in the volume averaged norm of the convective and pressure gradient forces as defined by Eq. 5, see Fig. 13. For this case the BCC packing does not follow the same trend as the other cases, indicating that this is not a general feature of the transition.
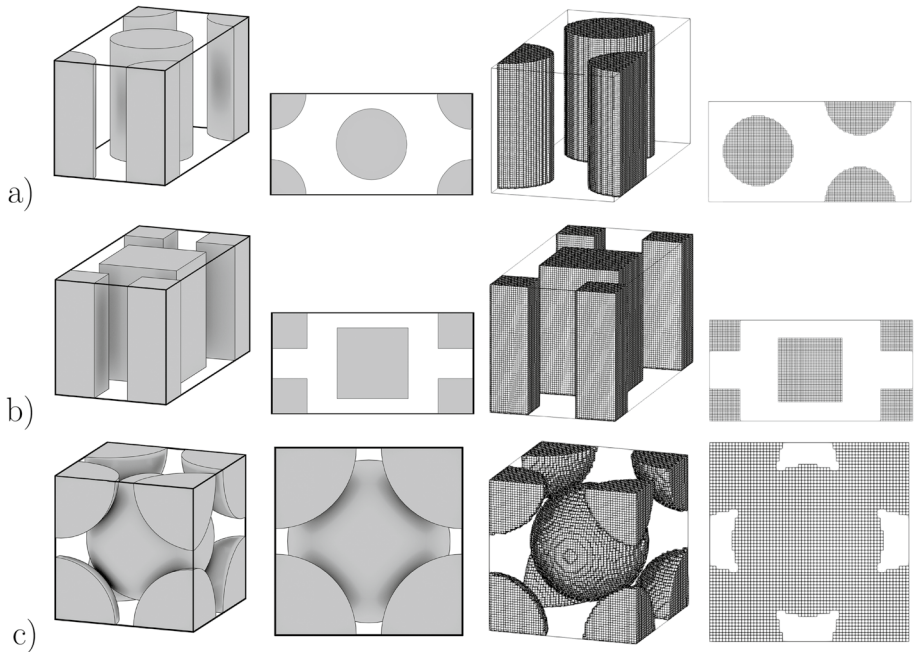
Fig. 7 The two columns to the left show the side 3D-views and top views of the geometries investigated for the transition. From top to bottom a staggered packing of cylinders (**a**), a staggered packing of quadratic rods (**b**) and a BCC packing of spheres (**c**). The meshes for respective case can be seen in the two columns to the right (side 3D-views and top views)

4.3 Quantifying the Transition Onset

It is expected that the deviation of the flow around the impinging solid surfaces reduces the pressure build-up at the front of the obstruction, therefore it can be hypothesized that a

Table 3 Summary of the specified simulation parameters for the transition investigation sweeps

Parameter	Cylinder	Rod	BCC
$(n_x n_y n_z)$	$(128 \times 64 \times 64)$	$(128 \times 64 \times 64)$	$(64 \times 64 \times 64)$
D_p	44.8	42	48.5
ϕ	0.614	0.590	0.544
$\nu(n)$	$0.05\left(\frac{0.0038}{0.05}\right)^{\frac{n}{N_n-1}}$	$0.05\left(\frac{0.004}{0.05}\right)^{\frac{n}{N_n-1}}$	$0.01\left(\frac{0.001}{0.01}\right)^{\frac{n}{N_n-1}}$
$\alpha(n)$	$0.05\left(\frac{0.0038}{0.05}\right)^{\frac{n}{N_n-1}}$	$0.05\left(\frac{0.004}{0.05}\right)^{\frac{n}{N_n-1}}$	$0.01\left(\frac{0.001}{0.01}\right)^{\frac{n}{N_n-1}}$
β	0.0125	0.0125	0.0125
F_x	3×10^{-6}	3×10^{-6}	10^{-6}
S	10^{-5}	10^{-5}	10^{-5}
T_w	0	0	0
Δt	1	1	1
N_n	50	50	50
N_t	400000	400000	400000

Fig. 8 The variation of the
dimensionless pressure drop p^*
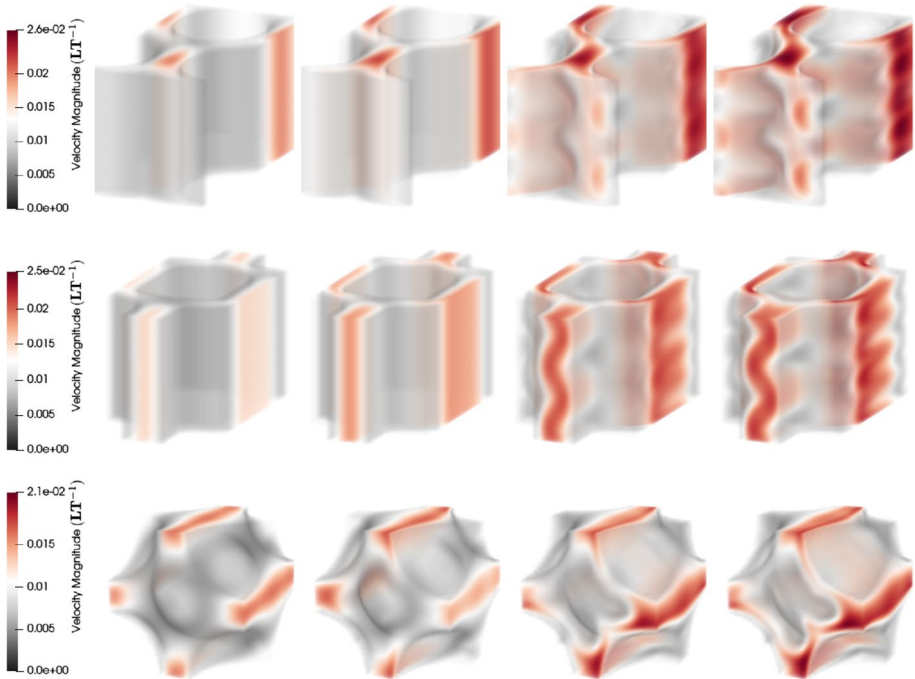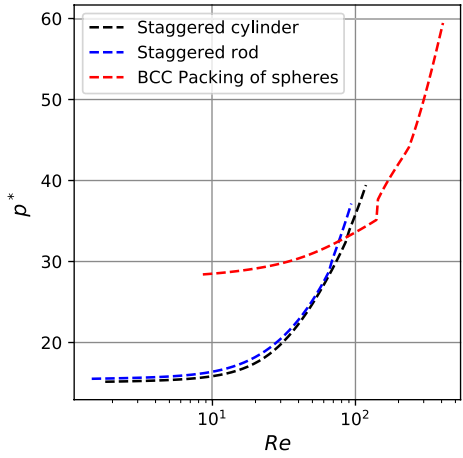with Re for all flow geometries

Fig. 9 The flow field change at the discontinuities visualized by a volume rendering of the velocity magnitude with increasing Reynolds number from left to right. From top to bottom the cases are for the staggered cylinder case, the staggered rod case and BCC packing. For the staggered cylinder case (top) the values of Re are from left to right $\{30, 50, 90, 120\}$, for the staggered rod case (middle) the values are $\{25, 40, 70, 90\}$ and for the BCC case (bottom) $\{120, 190, 320, 410\}$

Fig. 10 The spatial standard
deviation of absolute velocity in
the critical *Re* range scaled by
interstitial velocity U_{int} for the
staggered cylinder case (**a**), the
staggered quadratic rod case (**b**)
and the BCC packing (**c**)
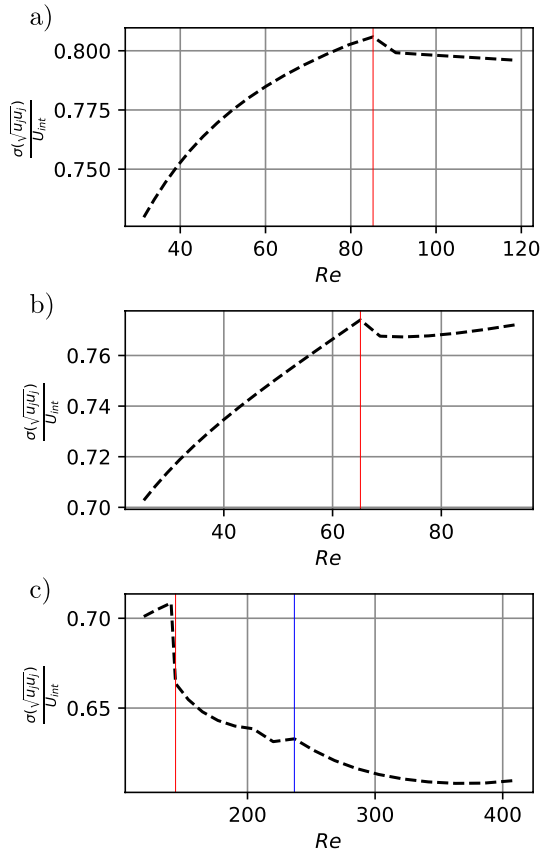
useful quantity for recognizing the onset is to watch for a transition in the pressure integral
across the solid surfaces. This integral can be written

$$p_{solid} = \left(\int_{\partial\Omega} d(\partial\Omega) \right)^{-1} \int_{\partial\Omega} p \, d(\partial\Omega) \tag{23}$$

where p is the pressure and $\partial\Omega$ is the solid–liquid boundary. The value of p_{solid} changes sig-
nificantly at the transition, see Fig. 14. This discontinuity in pressure surrounding the solid
surfaces indicate that the inertial cores no longer impinge the solid structures to the same
extent as previously. For the BCC packing, the first transition reduces the value of p_{solid}
while the second transition increases it. This indicates that the first transition for the BCC
packing may be of a fundamentally different type compared to the other transitions.

4.4 Impact on Heat Transfer Properties

Since the transition coincides with an increase of the resistance and small-scale struc-
tures of the flow, it can be expected that this would yield better heat transfer properties,
similar to what is seen for the transition to turbulence in porous media (Abraham et al.
2011). From observing Fig. 15 it is clear that the heat transfer is significantly impaired

Fig. 11 The dimensionless pressure drop variation in the critical Re range for the staggered cylinder case (**a**), the staggered quadratic rod case (**b**) and the BCC packing (**c**)

a)

b)

c)
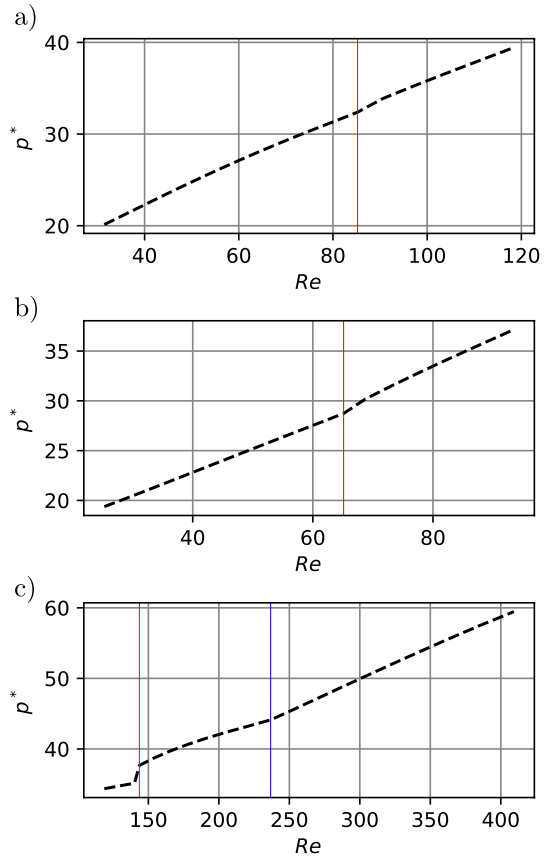
for both the staggered cylinder and BCC case but very slightly improves for the staggered rod case. It is therefore not possible to draw any general conclusions about how the transition will impact the heat transfer properties as it is geometry dependent. It can, however, be concluded that the transition can, significantly, affect the heat transfer.

5 Conclusions and Future Work

The flow fields of steady-state inertial transitions which occur across a wide range of high-tortuosity porous media has been scrutinized and a quantity which characterizes the transition has been proposed namely the pressure integral across the solid surfaces. The transition can, significantly, affect the heat transfer but also has some impact on all variables investigated which indicates a significant change in general flow characteristics. The BCC geometry case indicates that the transition can occur in systems similar to packed beds, which should be investigated explicitly in future studies. In addition to this a deepened study should be carried out on how the tortuosity of the porous bed impacts the possibility of the transition occurring.

Fig. 12 The fraction of pressure gradient forces to viscous forces in the *x*-direction of the critical Re range for the staggered cylinder case (**a**), the staggered quadratic rod case (**b**) and the BCC packing (**c**)
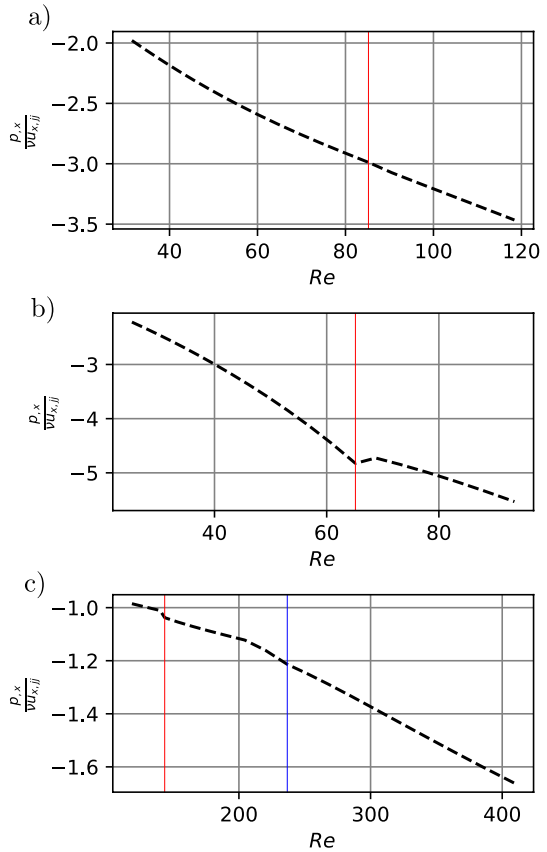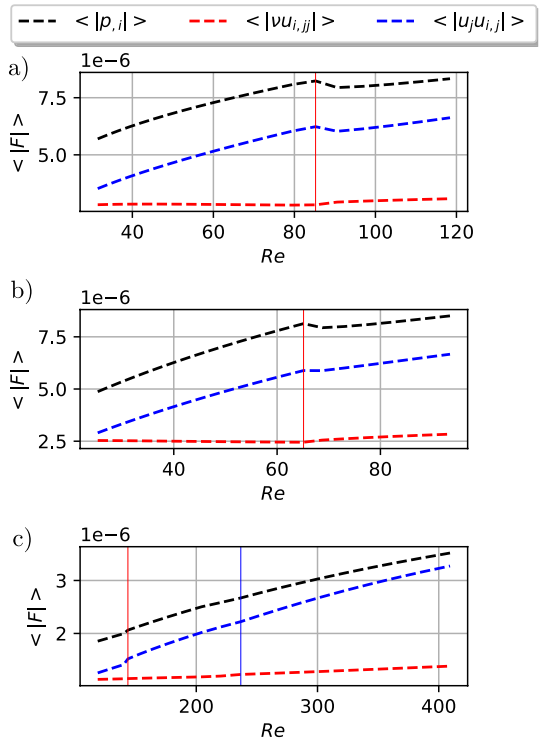

Appendix A—FDM Solver Implementation

The FDM solver used in this study utilizes central differences on an equidistant grid where the pressure and velocity nodes are collocated. The code is implemented in the CUDA framework and the source code is made publically available under a free license at *https://gitlab.com/c8383/gpu-fdm*. Since unitary time and spatial steps are used for all variables $\Delta x = \Delta y = \Delta z = \Delta t = 1$ and will therefore be omitted in the algorithm description. A field variable ϕ at position x, y, z and time t in the equidistant collocated grid is denoted by $\phi^t_{x,y,z}$. If the variable is a vector, such as the velocity u_i, it is denoted as $u^t_{i,(x,y,z)}$. The velocities will occasionally be referred to by their coordinate direction, i.e. $u_0 = u_x$, $u_1 = u_y$ and $u_2 = u_z$. Modular arithmetic is applied for the position coordinate at all boundaries and the mapping of the computational kernel should be interpreted accordingly.

Momentum Equation Discretization

Starting from (14) and applying central derivatives to all spatial quantities and a first-order Euler-forward in time the following update rule is obtained for the $u^{t+1}_{i,(x,y,z)}$ velocity

Fig. 13 The volume averaged norm of the force for the cylinder case (**a**), quadratic rod case (**b**) and BCC structure (**c**)

$$u^{t+1}_{i,(x,y,z)} = u^t_{i,(x,y,z)} + v\left(u^t_{i,(x-1,y,z)} - 2u^t_{i,(x,y,z)} + u^t_{i,(x+1,y,z)}\right) + \dots$$

$$v\left(u^t_{i,(x,y-1,z)} - 2u^t_{i,(x,y,z)} + u^t_{i,(x,y+1,z)}\right) + \dots$$

$$v\left(u^t_{i,(x,y,z-1)} - 2u^t_{i,(x,y,z)} + u^t_{i,(x,y,z+1)}\right) + \dots$$

$$-\frac{1}{2}u_x\left(u^t_{i,(x+1,y,z)} - u^t_{i,(x-1,y,z)}\right) + \dots$$

$$-\frac{1}{2}u_y\left(u^t_{i,(x,y+1,z)} - u^t_{i,(x,y-1,z)}\right) + \dots \tag{24}$$

$$-\frac{1}{2}u_z\left(u^t_{i,(x,y,z+1)} - u^t_{i,(x,y,z-1)}\right) + \dots$$

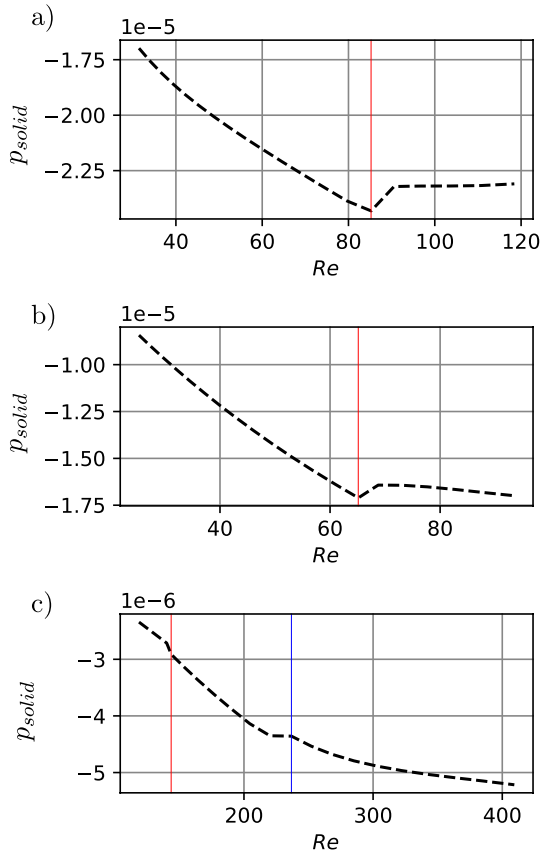$$-\frac{1}{2\rho}p_{,i} + \frac{1}{\rho}F_i.$$

Where the last term $p_{,i}$ depends on the index i and is equal to

$$p_{,x} = p^t_{x+1,y,z} - p^t_{x-1,y,z} \tag{25}$$

$$p_{,y} = p^t_{x,y+1,z} - p^t_{x,y-1,z} \tag{26}$$

$$p_{,z} = p^t_{x,y,z+1} - p^t_{x,y,z-1}. \tag{27}$$

Fig. 14 The pressure integral on the solid boundary for the cylinder case (**a**), quadratic rod case (**b**) and BCC packing (**c**)
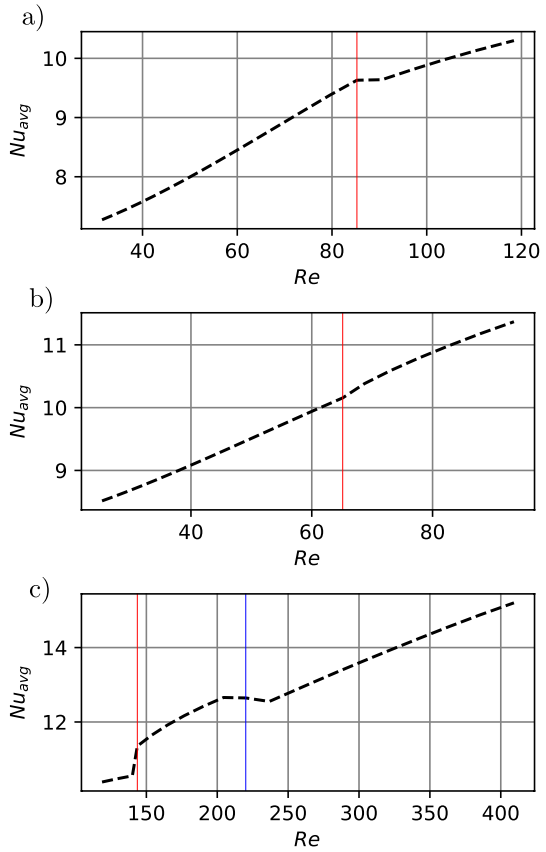

Pressure Correction Discretization

The expression to obtain the updated pressure correction $p_{x,y,z}^{t+1}$ is based on a second-order accurate central derivative discretization of (15) with an advection term added, the expression becomes

$$
\begin{aligned}
p_{x,y,z}^{t+1} = p_{x,y,z}^{t} &+ \beta\left(u_{x,(x+1,y,z)}^{t} - u_{x,(x-1,y,z)}^{t}\right) + \dots \\
\beta\left(u_{y,(x,y+1,z)}^{t} - u_{y,(x,y-1,z)}^{t}\right) &+ \dots \\
\beta\left(u_{z,(x,y,z+1)}^{t} - u_{z,(x,y,z+1)}^{t}\right) &+ \dots \\
-\frac{1}{2}u_x\left(p_{x+1,y,z}^{t} - p_{x-1,y,z}^{t}\right) &+ \dots \\
-\frac{1}{2}u_y\left(p_{x,y+1,z}^{t} - p_{x,y-1,z}^{t}\right) &+ \dots \\
-\frac{1}{2}u_z\left(p_{x,y,z+1}^{t} - p_{x,y,z-1}^{t}\right). &
\end{aligned}
\tag{28}
$$

Fig. 15 The variation of the average Nusselt number Nu_{avg} for $Pr = 1$ with Re for the staggered cylinder case (**a**), staggered rod case (**b**) and BCC case (**c**). The transition regions are marked by the vertical lines

Advection Diffusion Equation Discretization

The expression to obtain the updated species concentration or thermal value depending on interpretation of the variable T is based on a second-order accurate central derivative discretization of (17), the expression becomes

$$
\begin{aligned}
T^{t+1}_{x,y,z} = T^{t}_{x,y,z} &+ \alpha\left(T^{t}_{x-1,y,z} - 2T^{t}_{x,y,z} + T^{t}_{x+1,y,z}\right) + \ldots \\
\alpha\left(T^{t}_{x,y-1,z} - 2T^{t}_{x,y,z} + T^{t}_{x,y+1,z}\right) &+ \ldots \\
\alpha\left(T^{t}_{x,y,z-1} - 2T^{t}_{x,y,z} + T^{t}_{x,y,z+1}\right) &+ \ldots \\
-\frac{1}{2}u_x\left(T^{t}_{x+1,y,z} - T^{t}_{x-1,y,z} + T_{Gx}\right) &+ \ldots \\
-\frac{1}{2}u_y\left(T^{t}_{x,y+1,z} - T^{t}_{x,y-1,z} + T_{Gy}\right) &+ \ldots \\
-\frac{1}{2}u_z\left(T^{t}_{x,y,z+1} - T^{t}_{x,y,z-1} + T_{Gz}\right) &+ S.
\end{aligned}
\tag{29}
$$

Pressure Smoothing Discretization

The pressure smoothing as described by (16) increases numerical stability and reduces checkerboarding. For this operation a second-order accurate central derivative discretization is used for the spatial differences and a first-order accurate Euler-forward temporal discretization

$$
\begin{aligned}
p_{x,y,z}^{t+1} = p_{x,y,z}^{t} + S_p \frac{1}{12} \Big[& \dots \\
\left(1 - W_{x-1,y,z}\right) \times \left(p_{x-1,y,z}^{t} - p_{x,y,z}^{t}\right) + & \dots \\
\left(1 - W_{x+1,y,z}\right) \times \left(p_{x+1,y,z}^{t} - p_{x,y,z}^{t}\right) + & \dots \\
\left(1 - W_{x,y-1,z}\right) \times \left(p_{x,y-1,z}^{t} - p_{x,y,z}^{t}\right) + & \dots \\
\left(1 - W_{x,y+1,z}\right) \times \left(p_{x,y+1,z}^{t} - p_{x,y,z}^{t}\right) + & \dots \\
\left(1 - W_{x,y,z-1}\right) \times \left(p_{x,y,z-1}^{t} - p_{x,y,z}^{t}\right) + & \dots \\
\left(1 - W_{x,y,z+1}\right) \times \left(p_{x,y,z+1}^{t} - p_{x,y,z}^{t}\right) & \Big].
\end{aligned}
\tag{30}
$$

Where the variable $W_{x,y,z}$ is the wall coordinate which is 1 if the element is a wall and 0 otherwise.
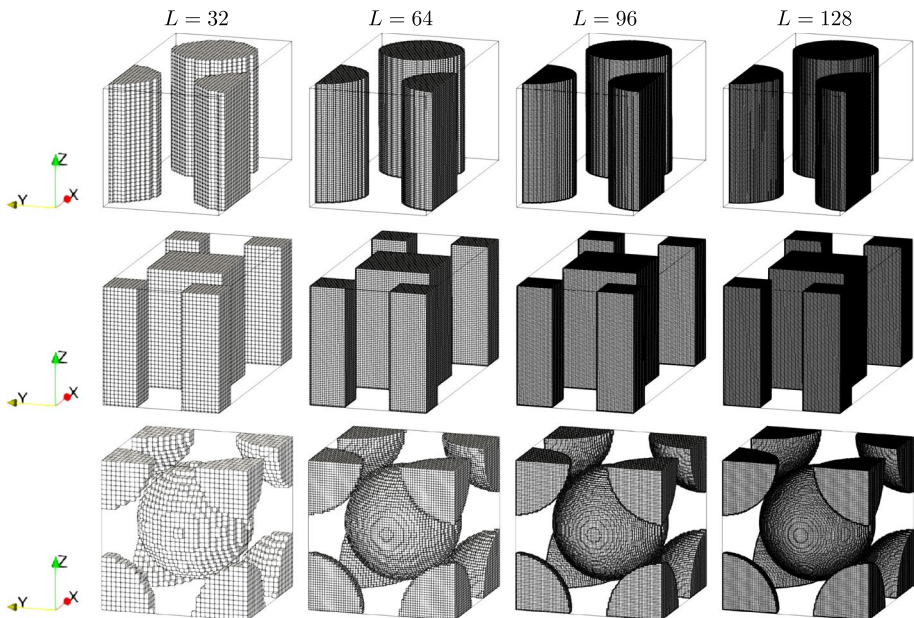

Fig. 16 The meshes, from top to bottom the staggered cylinder case, the staggered quadratic case and the BCC packing of spheres

Order of Operations and Wall Treatment

The order of operations is as follows, for the main kernel the momentum update, pressure correction update and advection diffusion update are applied to the state of the field variables at time $t + 1$ using the variables at time t. Following this n sweeps of the pressure smoothing operation is applied, for the cases presented in this article $n = 1$. Wall elements are treated as constant value elements for all field variables except for the pressure correction equation.

Appendix B—Impact of Grid Resolution

In this section a grid sensitivity analysis is presented, four grid sizes are investigated for each geometry denoted by the short-side side length element count L, see Fig. 16. The numerical values used for the calculations are presented in Tables 4, 5 and 6. Due to the step-wise approximation of the geometry the porosity ϕ varies between the cases. The results converge well across all cases presented in Fig. 17 which are the dimensionless pressure drop p^*, the surface integral of the pressure across the boundaries p_{solid} and the Nusselt number Nu_{avg}.

Table 4 Summary of the specified simulation parameters for the staggered cylinder mesh study

Resolution	$L = 32$	$L = 64$	$L = 96$	$L = 128$
$(n_x n_y n_z)$	$(64 \times 32 \times 32)$	$(128 \times 64 \times 64)$	$(192 \times 96 \times 96)$	$(256 \times 128 \times 128)$
D_p	22.4	44.8	67.2	89.6
ϕ	0.608	0.614	0.615	0.615
$v(n)$	$0.025\left(\frac{0.0038}{0.05}\right)^{\frac{n}{N_n-1}}$	$0.05\left(\frac{0.0038}{0.05}\right)^{\frac{n}{N_n-1}}$	$0.075\left(\frac{0.0038}{0.05}\right)^{\frac{n}{N_n-1}}$	$0.1\left(\frac{0.0038}{0.05}\right)^{\frac{n}{N_n-1}}$
$\alpha(n)$	$0.025\left(\frac{0.0038}{0.05}\right)^{\frac{n}{N_n-1}}$	$0.05\left(\frac{0.0038}{0.05}\right)^{\frac{n}{N_n-1}}$	$0.075\left(\frac{0.0038}{0.05}\right)^{\frac{n}{N_n-1}}$	$0.1\left(\frac{0.0038}{0.05}\right)^{\frac{n}{N_n-1}}$
β	0.0125	0.0125	0.0125	0.0125
F_x	6×10^{-6}	3×10^{-6}	2×10^{-6}	1.5×10^{-6}
S	10^{-5}	10^{-5}	10^{-5}	10^{-5}
T_w	0	0	0	0
Δt	1	1	1	1
N_n	50	50	50	50
N_t	200000	400000	600000	800000

Table 5 Summary of the specified simulation parameters for the staggered quadratic rod mesh study

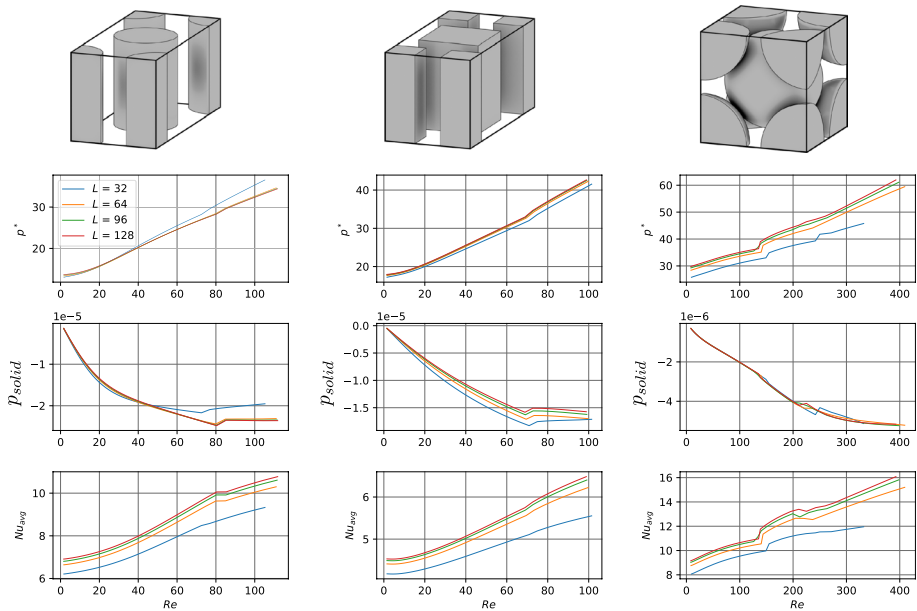| Resolution	$L = 32$	$L = 64$	$L = 96$	$L = 128$
$(n_x n_y n_z)$	$(64 \times 32 \times 32)$	$(128 \times 64 \times 64)$	$(192 \times 96 \times 96)$	$(256 \times 128 \times 128)$
D_p	21	42	63	84
ϕ	0.569	0.590	0.596	0.6
$\nu(n)$	$0.025\left(\frac{0.004}{0.05}\right)^{\frac{n}{N_n-1}}$	$0.05\left(\frac{0.004}{0.05}\right)^{\frac{n}{N_n-1}}$	$0.075\left(\frac{0.004}{0.05}\right)^{\frac{n}{N_n-1}}$	$0.1\left(\frac{0.004}{0.05}\right)^{\frac{n}{N_n-1}}$
$\alpha(n)$	$0.025\left(\frac{0.004}{0.05}\right)^{\frac{n}{N_n-1}}$	$0.05\left(\frac{0.004}{0.05}\right)^{\frac{n}{N_n-1}}$	$0.075\left(\frac{0.004}{0.05}\right)^{\frac{n}{N_n-1}}$	$0.1\left(\frac{0.004}{0.05}\right)^{\frac{n}{N_n-1}}$
β	0.0125	0.0125	0.0125	0.0125
F_x	6×10^{-6}	3×10^{-6}	2×10^{-6}	1.5×10^{-6}
S	10^{-5}	10^{-5}	10^{-5}	10^{-5}
T_w	0	0	0	0
Δt	1	1	1	1
N_n	50	50	50	50
N_t	200000	400000	600000	800000

Table 6 Summary of the specified simulation parameters for the BCC packing mesh study

Resolution	$L = 32$	$L = 64$	$L = 96$	$L = 128$
$(n_x n_y n_z)$	$(32 \times 32 \times 32)$	$(64 \times 64 \times 64)$	$(96 \times 96 \times 96)$	$(128 \times 128 \times 128)$
D_p	24.25	48.5	72.75	97
ϕ	0.546	0.544	0.545	0.544
$\nu(n)$	$0.005\left(\frac{0.001}{0.01}\right)^{\frac{n}{N_n-1}}$	$0.01\left(\frac{0.001}{0.01}\right)^{\frac{n}{N_n-1}}$	$0.015\left(\frac{0.001}{0.01}\right)^{\frac{n}{N_n-1}}$	$0.02\left(\frac{0.001}{0.01}\right)^{\frac{n}{N_n-1}}$
$\alpha(n)$	$0.005\left(\frac{0.001}{0.01}\right)^{\frac{n}{N_n-1}}$	$0.01\left(\frac{0.001}{0.01}\right)^{\frac{n}{N_n-1}}$	$0.015\left(\frac{0.001}{0.01}\right)^{\frac{n}{N_n-1}}$	$0.02\left(\frac{0.001}{0.01}\right)^{\frac{n}{N_n-1}}$
β	0.0125	0.0125	0.0125	0.0125
F_x	2×10^{-6}	10^{-6}	0.75×10^{-6}	0.5×10^{-6}
S	10^{-5}	10^{-5}	10^{-5}	10^{-5}
T_w	0	0	0	0
Δt	1	1	1	1
N_n	50	50	50	50
N_t	200000	400000	600000	800000

Fig. 17 The results from the mesh comparison study

Data availability The datasets generated and analysed during the current study are available from the corresponding author on reasonable request. The source code for the solver used in this study is publically available via the link https://gitlab.com/c8383/gpu-fdm.

Declarations

Conflict of interest The authors have no relevant financial or non-financial interests to disclose.

References

Abbaszadeh, M., Salehi, A., Abbassi, A.: Lattice boltzmann simulation of heat transfer enhancement in an asymmetrically heated channel filled with random porous media. J. Porous Media **20**(2) (2017)

Abraham, J., Sparrow, E., Minkowycz, W.: Internal-flow nusselt numbers for the low-reynolds-number end of the laminar-to-turbulent transition regime. Int. J. Heat Mass Transf. **54**(1–3), 584–588 (2011)

Bear, J.: Dynamics of Fluids in Porous Media (1972)

Burstrom, P.E.C., Frishfelds, V., Ljung, A.-L., Lundstrom, T.S., Marjavaara, B.D.: Modelling heat transfer during flow through a random packed bed of spheres. Heat Mass Transf. **54**, 1225–1245 (2018)

Chu, X., Yang, G., Pandey, S., Weigand, B.: Direct numerical simulation of convective heat transfer in porous media. Int. J. Heat Mass Transf. **133**(April), 11–20 (2019)

Farzaneh, M., Strom, H., Zanini, F., Carmignato, S., Sasic, S., Maggiolo, D.: Pore-scale transport and two-phase fluid structures in fibrous porous layers: application to fuel cells and beyond. Transp. Porous Media **136**, 245–270 (2021)

Ferziger J.H., Perić, M., Street, R.L.: Computational Methods for Fluid Dynamics, vol. 3. Springer (2002)

Forslund, T.O., Larsson, I., Lycksam, H., Hellström, J.G.I., Lundström, T.S.: Non-stokesian flow through ordered thin porous media imaged by tomographic-piv. Exp. Fluids **62**(3), 1–12 (2021)

Forslund, T.O., Larsson, I., Hellström, J.G.I., Lundström, T.S.: The effects of periodicity assumptions in porous media modelling. Transp. Porous Media **137**(3), 769–797 (2021)

Foudhil, W., Dhifaoui, B., Jabrallah, S.B., Belghith, A., Corriou, J.P.: Numerical and experimental study of convective heat transfer in a vertical porous channel using a non-equilibrium model. J. Porous Media **15**(6) (2012)

Frishfelds, V., Hellström, J.G., Lundström, T.S., Mattsson, H.: Fluid flow induced internal erosion within porous media: modelling of the no erosion filter test experiment. Transp. Porous Media **89**(3), 441–457 (2011)

Jin, Y., Uth, M.F., Kuznetsov, A.V., Herwig, H.: Numerical investigation of the possibility of macroscopic turbulence in porous media: a direct numerical simulation study. J. Fluid Mech. **766**, 76–103 (2015)

Johns, M., Sederman, A., Bramley, A., Gladden, L., Alexander, P.: Local transitions in flow phenomena through packed beds identified by mri. AIChE J. **46**(11), 2151–2161 (2000)

Jouybari, N.F., Lundstrom, T.S., Hellstrom, J.G.I.: Investigation of thermal dispersion and intra-pore turbulent heat flux in porous media. Int. J. Heat Fluid Flow **81** (2020)

Jouybari, N.F., Lundstrom, T.S.: Investigation of post-darcy flow in thin porous media. Transp. Porous Media **138**, 157–184 (2021)

Khayamyan, S., Lundström, T.S., Hellström, J.G.I., Gren, P., Lycksam, H.: Measurements of transitional and turbulent flow in a randomly packed bed of spheres with particle image velocimetry. Transp. Porous Media **116**(1), 413–431 (2017)

Khayamyan, S., Lundström, T.S., Gren, P., Lycksam, H., Hellström, J.G.I.: Transitional and turbulent flow in a bed of spheres as measured with stereoscopic particle image velocimetry. Transp. Porous Media **117**(1), 45–67 (2017)

Koch, D.L., Ladd, A.J.: Moderate Reynolds number flows through periodic and random arrays of aligned cylinders. J. Fluid Mech. **349**, 31–66 (1997)

Kwak, D., Kiris, C.C.: Computation of viscous incompressible flows (2011)

Larsson, I.A., Lundström, T.S., Lycksam, H.: Tomographic PIV of flow through ordered thin porous media. Exp. Fluids **59**(6), 3–8 (2018)

Lu, J., Jang, H.K., Lee, S.B., Hwang, W.R.: Characterization on the anisotropic slip for flows over unidirectional fibrous porous media for advanced composites manufacturing. Compos. Part A Appl. Sci. Manuf. **100**, 9–19 (2017)

Lundstrom, T.S., Hellstrom, J.G.I., Jonsson, P.J.P.: Laminar and turbulent flow through an array of cylinders. J. Porous Media **13**(12), 1073–1085 (2010)

Moosavi, A., Ljung, A.-L., Lundstrom, T.S.: Design considerations to prevent thermal hazards in cylindrical lithium-ion batteries: an analytical study. J. Energy Storage **38** (2021)

Nguyen, T., Kappes, E., King, S., Hassan, Y., Ugaz, V.: Time-resolved piv measurements in a low-aspect ratio facility of randomly packed spheres and flow analysis using modal decomposition. Exp. Fluids **59** (2018)

Odabaee, M., Hooman, K.: Metal foam heat exchangers for heat transfer augmentation from a tube bank. Appl. Therm. Eng. **36**, 456–463 (2012)

Patil, V.A., Liburdy, J.A.: Turbulent flow characteristics in a randomly packed porous bed based on particle image velocimetry measurements. Phys. Fluids **25**(4) (2013)

Rao, F., Jin, Y.: Possibility for survival of macroscopic turbulence in porous media with high porosity. J. Fluid Mech. **937**, 1–23 (2022)

Rybiński, W., Mikielewicz, J.: Analytical solutions of heat transfer for laminar flow in rectangular channels. Arch. Thermodyn. **35**(4), 29–42 (2014)

Seguin, D., Montillet, A., Comiti, J.: Experimental characterisation of flow regimes in various porous media-II transition to turbulent regime. Chem. Eng. Sci. **53**(22), 3897–3909 (1998)

Seguin, D., Montillet, A., Comiti, J.: Experimental charecterisation of flow regimes in various porus media - I: limit of laminar flow regime. Chem. Eng. Sci. **53**(21), 3751–3761 (1998)

Tan, H., Pillai, K.M.: Multiscale modeling of unsaturated flow in dual-scale fiber preforms of liquid composite molding i: isothermal flows. Compos. Part A Appl. Sci. Manuf. **43**, 1–13 (2012)

Tan, H., Pillai, K.M.: Multiscale modeling of unsaturated flow of dual-scale fiber preform in liquid composite molding ii: non-isothermal flows. Compos. Part A Appl. Sci. Manuf. **43**, 14–28 (2012)

Tan, H., Pillai, K.M.: Multiscale modeling of unsaturated flow in dual-scale fiber preforms of liquid composite molding iii: reactive flows. Compos. Part A Appl. Sci. Manuf. **43**, 29–44 (2012)

Uth, M.F., Jin, Y., Kuznetsov, A.V., Herwig, H.: A direct numerical simulation study on the possibility of macroscopic turbulence in porous media: effects of different solid matrix geometries, solid boundaries, and two porosity scales. Phys. Fluids **28** (2016)

Xu, Z., Pillai, K.M.: Modeling drying in thin porous media after coupling pore-level drying dynamics with external flow field. Dry. Technol. **35**(7), 785–801 (2017)

Yang, J., Zhou, M., Li, S.Y., Bu, S.S., Wang, Q.W.: Three-dimensional numerical analysis of turbulent flow in porous media formed by periodic arrays of cubic, spherical, or ellipsoidal particles. J. Fluids Eng. Trans. ASME **136** (2014)

Zarandi, M.A.F., Pillai, K.M., Hasan, A.B.M.R.: Investigating liquid-fronts during spontaneous imbibition of liquids in industrial wicks. Part ii: validation by dns. AICHE J